Carbon 242 (2025) 120378

Contents lists available at ScienceDirect

Carbon

journal homepage: www.elsevier.com/locate/carbon

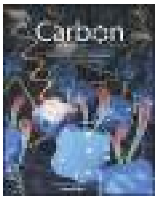

Reconfigurable high-temperature thermal protection shape memory aerogel based on phthalonitrile resin with facile template method

Rongxiang Hu[a], Fenghua Zhang[a,*], Lan Luo[a], Linlin Wang[a], Yanju Liu[b], Jinsong Leng[a,**]

[a] *Centre for Composite Materials and Structures, Harbin Institute of Technology (HIT), Harbin, 150080, People's Republic of China*
[b] *Department of Astronautical Science and Mechanics, Harbin Institute of Technology (HIT), Harbin, 150001, People's Republic of China*

ARTICLE INFO

Keywords:
Shape memory phthalonitrile resins
Aerogel
High-temperature resistance
Dynamic thermal protection
Microwave absorption

ABSTRACT

Shape memory polymer aerogels (SMPAs) hold great promise for aerospace thermal insulation but face high-temperature limitations. This study develops a phthalonitrile-based shape memory aerogel (SMPNA) through an in-situ polymerization template method, which exhibits remarkable compression resistance and low thermal conductivity due to its isotropic microporous structures. The shape recovery at high temperatures, based on its shape memory effect, allows SMPNA to provide dynamic thermal protection induced by its thermally driven deformation. The inherent high-temperature resistance of the matrix endows SMPNA with excellent thermal dimensional stability, exhibiting almost no shrinkage at 400 °C. In addition, after thermal treatment exceeds 600 °C, SMPNA undergoes carbonization while retains its microporous structure, thereby possessing excellent microwave absorption performance. The developed SMPNA integrates low-temperature insulation, high-temperature dynamic thermal protection, and microwave absorption capabilities after carbonization, broadening its application prospects. Furthermore, by incorporating multi-walled carbon nanotubes (MWCNTs), the SMPNA composite (SMPNAc) containing 8 % MWCNTs exhibits good microwave absorption characteristics that can be modulated via shape memory behavior. Additionally, the microwave absorption performance of SMPNAc remains stable across a broad temperature range up to 400 °C. This work offers new insights for the multi-functional applications of SMPAs in high-temperature environments.

1. Introduction

Shape memory polymers (SMPs) are a class of smart materials that can respond to external stimuli, such as light, heat, or electricity, allowing them to return from a programmed temporary shape to the original permanent shape [1–3]. The inherent stimuli-responsive property has facilitated the widespread application of SMPs across various fields, including aerospace, medical devices, sensors, and robotics, making them research hotspots in the field of advanced functional materials [4–7]. With the advancement of smart materials and structures, the design, fabrication, and engineering applications of SMPs are becoming increasingly diversified toward multifunctional capabilities, such as multi-stimuli-responsive SMPs [8–10], self-healing SMPs [11], and SMPs with multiple memory effects [12].

Aerogels represent a category of porous solid materials characterized by low density, high porosity, and large specific surface areas [13], which are widely applied in aerospace, thermal insulation, acoustic insulation, shock absorption, and energy storage devices [14–18]. In general, aerogels can be classified into organic aerogels and inorganic aerogels based on their composition [14]. Organic aerogels predominantly consist of polymers and confer excellent flexibility and elasticity, making them suitable for flexible insulation materials. In contrast, inorganic aerogels composed of metal oxides or silicides typically exhibit high stiffness and high-temperature resistance, making them suitable for high-temperature insulation and fire prevention applications. Once an aerogel is fabricated, its stiffness is usually difficult to alter.

Interestingly, SMPs demonstrate considerable stiffness below the deformation temperature and exhibit increased flexibility above this temperature. The advantages of SMPs and aerogels can be integrated into a novel smart material, shape memory polymer aerogels (SMPAs) [19], which not only possess the shape memory functions but also retain the low density and high porosity of aerogels, making them suitable for a wide range of complex application environments. Wu et al. integrated

---

* Corresponding author.
** Corresponding author.
E-mail addresses: fhzhang_hit@163.com (F. Zhang), lengjs@hit.edu.cn (J. Leng).

https://doi.org/10.1016/j.carbon.2025.120378
Received 21 March 2025; Received in revised form 30 April 2025; Accepted 30 April 2025

graphene oxide with a block copolymer, polystyrene-b-poly (ethylene-butylene)-b-polystyrene-g-maleic anhydride, to fabricate a hybrid SMPA with ultralow thermal conductivity, high mechanical properties, high hydrophobicity and zero Poisson's ratio [20]. This SMPA holds great potential for applications in the complex surfaces and confined spaces of buildings, industry and spacecraft. Liu et al. prepared shape memory polyimide composite aerogels with a high deformation temperature (280 °C) and excellent mechanical properties by using water-soluble polyamic acid and graphene oxide, which were processed through freeze-drying and thermal imidization [21]. These SMPAs are expected to find new applications in aerospace engineering.

The thermal stability of the aerogel matrix determines its applicable environment. Shape memory phthalonitrile resin (SMPN) has been confirmed as a high-thermal-stability smart material in our previous research [22], which shows broad application prospects in harsh high-temperature environments. In this work, a SMPN-based aerogel (SMPNA) was prepared via a facile in-situ polymerization templating method using NaCl as the template. During the fabrication process, SMPNA formed a rich porous morphology with negligible volume shrinkage. The SMPNA exhibited a low density of 0.134 g/cm^3 and a porosity of 88.8 %, demonstrating low thermal conductivity at both room temperature and 300 °C. Owing to its variable stiffness characteristic, the SMPNA can be fixed to a temporary shape compressed to 40 % of its initial height, thereby adjusting its thermal conductivity from 37.32 to 46.64 mW/m·K. The shape memory effect also endows SMPNA with dynamic thermal protection under the butane flame. In addition, the high thermal stability of the matrix endows the SMPNA with exceptional thermal dimensional stability with almost no shrinkage below temperatures of 400 °C, and maintains a linear shrinkage rate within 20 % even at elevated temperatures reaching up to 1000 °C, providing a guarantee for the stable use of the aerogel structure in high-temperature environments. Following high-temperature pyrolysis, the aerogel undergoes carbonization and attains electrical conductivity, allowing it to function effectively as a microwave-absorbing material, which further broadens the scope of potential applications for SMPNAs under extreme temperature conditions.

2. Experimental

2.1. Materials

All reagents and solvents were used as received without any purification. Bisphenol A, 4,4′-difluorodiphenylmethanone, 4-nitrophthalonitrile, 4-phenylphenol, anhydrous potassium carbonate (K_2CO_3), phenol bis[4-(3-aminophenoxy)phenyl] sulfone, and NaCl were purchased from Shanghai Aladdin Biochemical Technology Co., Ltd. Toluene and dimethyl sulfoxide (DMSO) were supplied by Tianjin Guangfu Chemical Reagent Factory. The MWCNTs were acquired from Chengdu Jiacai Technology Co., Ltd.

2.2. Preparation of monomers and B-stage SMPN

The end-capping reagent and monomer of SMPN were synthesized following the procedures reported in our previous work [22], with specific preparation details available in the supplementary materials. The prepolymer was blended with the curing agent *m*-BAPS at a concentration of 5 wt%, heated to 230 °C for 0.5 h, and subsequently cooled to obtain B-stage SMPN.

2.3. Preparation of SMPNAs

The B-stage SMPN was smashed via a high-speed pulverizer, and NaCl granules were then added and mixed thoroughly. The uniformly mixed powder was placed into the mold of a tablet press and compressed at 25 MPa for molding. Following this step, the sample was removed and transferred to a high-temperature oven for in-situ postcuring polymerization through a stepwise temperature increase regimen, specifically, 260 °C/4h, 280 °C/4h, 300 °C/4h, 325 °C/4h, 350 °C/4h. Afterward, the sample was taken out and placed in water to dissolve the NaCl template, and then dried to obtain the SMPN-based aerogel. The samples were labeled according to the concentration of SMPN matrix as A5, A10, A15, A20 and A25, and the details can be found in Table 1.

2.4. Characterization

Fourier transform infrared (FTIR) spectra were recorded using a Spectrum Two DGTS instrument (PerkinElmer, MA, USA). Scanning electron microscopy (SEM) images were obtained using a TESCAN AMBER. The Brunauer–Emmett–Teller (BET) method was used to calculate the specific surface area with a V-Sorb 4800 TP analyzer. The thermal conductivity was characterized via a Hot Disk TPS 2500S. Thermogravimetric analysis (TGA) test of SMPNA was performed on a Mettler–Toledo TGA/DSC STARe System at a heating rate of 10 °C/min over a temperature range from 25 °C to 1000 °C in N_2. Dynamic mechanical analysis (DMA) was performed using a Q800 (TA Instruments) to investigate the thermodynamic properties of the SMPNA. The pore size distribution was tested by Micromeritics Mercury Porosimetry Analysis (MicroActive AutoPore V 9600). The Raman spectra were acquired using a Laser confocal Raman Spectrometer (Thermo Scientific DXR2xi).

Porosity Calculation: The apparent density (ρ_a) was determined by measuring the mass and volume of the aerogels. The skeletal density (ρ_s) was calculated based on the mass and volume of the SMPN. The Porosity (η) of SMPNA was then calculated by Eq. (1):

$$\eta = \left(1 - \frac{\rho_a}{\rho_s}\right) \times 100\% \tag{1}$$

Electromagnetic Parameters Test: The thermally-treated SMPNAs were pressed into a coaxial ring with an inner diameter of 3 mm. Electromagnetic parameters were obtained through the coaxial method with a Vector Network Analyzers (VNA, Agilent E5071C) within the frequency range of 1–18 GHz, and the reflection loss (RL) values were calculated based on transmission line theory, as expressed in Equations (2) and (3):

$$Z_{in} = Z_0\sqrt{\frac{\mu_r}{\varepsilon_r}}\tanh\left(j\left(\frac{2\pi fd}{c}\right)\sqrt{\mu_r\varepsilon_r}\right) \tag{2}$$

$$RL(dB) = 20\lg\left|\frac{Z_{in} - Z_0}{Z_{in} + Z_0}\right| \tag{3}$$

3. Results and discussion

3.1. Preparation and structural characterization of the SMPNA

Using the SMPN prepared by the end-capping strategy as the matrix and NaCl as the template, the preparation process of SMPNA is illustrated in Fig. 1a and b. The prepared SMPNAs were labeled according to the resin matrix content. Specifically, A5 denotes a template mixture containing 5 wt% SMPN, with similar nomenclature applied to other samples. The chemical structure of the resulting SMPNA was characterized using FTIR spectroscopy. As shown in Fig. 1c, all the sample exhibited a characteristic cross-linked PN resin structure, with an absorption peak at 1718 cm^{-1} corresponding to the isoindoline, the peaks at 1509 cm^{-1} and 1358 cm^{-1} corresponding to the triazine ring, and the

Table 1
The content of the samples.

Sample	A5	A10	A15	A20	A25
SMPN matrix content	5 %	10 %	15 %	20 %	25 %
Template content	95 %	90 %	85 %	80 %	75 %

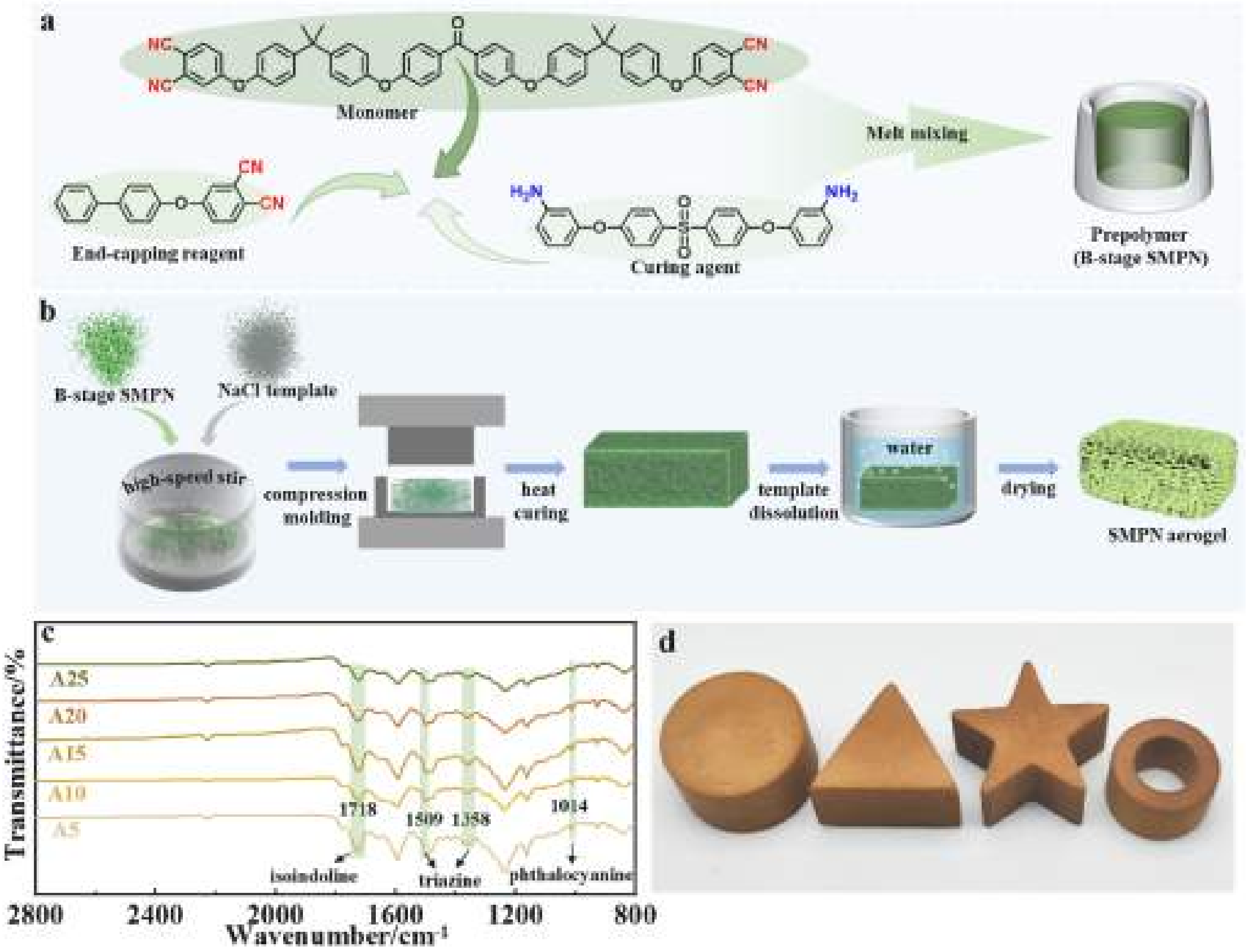

Fig. 1. Preparation of a) B-stage SMPN and b) SMPNA. c) FTIR spectrum of obtained aerogels. d) Photograph of SMPNA with different shapes.

peak at 1014 cm^{-1} corresponding to the phthalocyanine. The template content has almost no effect on the chemical structure of the SMPN resin matrix, but significantly influences the dimensional stability of the samples. Higher levels of template content reduce the flowability of the molten mixture, thereby aiding in shape retention during the post-curing process. The lower template content observed in sample A25 led to plastic deformation prior to matrix curing. The A5 sample contains a relatively large amount of template and a small amount of the SMPN matrix. After the templates were removed by water washing, the aerogel underwent a certain degree shrinkage during the drying process (Fig. S1). Thus, only samples A10, A15 and A20 demonstrated adequate dimensional stability in the process of in-situ polymerization template preparation of aerogels.

Table 2 lists the physical properties associated with these aerogels. The obtained aerogels demonstrate a low density ranging from 0.1 g/cm^3 to 0.3 g/cm^3. In addition, the cured samples can be machined into various shapes prior to template removal. An aerogel of the desired shape is achievable after template removal (Fig. 1d), thereby enhancing the diversity of available aerogel forms.

The SEM was used to investigate the micromorphology of the materialsa, and Fig. S2 shows the microstructures of the template and B-stage SMPN powder. The template and prepolymer powders both exhibit irregular morphologies due to random collisions caused by high-speed pulverization. Fig. S3 shows SEM images of the samples containing NaCl template and SMPN matrix after compression molding and post-curing. Fig. 2a and b illustrate the micromorphology of the aerogels before and after removal of the template. The uneven particle size of NaCl in the composite, resulting from random fragmentation during high-speed mixing process, leads to the formation of irregular pores in the aerogel after the template is dissolved. The EDS map in Fig. 2a indicates that as the content of the template decreases, the interface between the resin matrix and template becomes increasingly discernible. There is almost no visible interface between the matrix and its corresponding template in sample A10 with high template content due to nearly complete coverage with NaCl particles, as shown in the EDS mapping. As the matrix content increases and the template content decreases, NaCl particles can be identified within EDS analysis for samples A15, and in A20, in which the template gaps are filled with the resin matrix., Fig. 2b shows the abundant porous structure of the aerogels after the template removal. The pore microstructure associated with sample A10 appears relatively loose with thin pore walls. As the matrix content increases, the samples A15 and A20 becomes more compact and display increased density along with thicker pore walls, which favor to

Table 2
The physical properties of the obtained aerogels.

Sample	Density (g/cm^3)	Porosity (%)	Pore Volume (cm^3/g)
A10	0.13	88.8	1.90
A15	0.19	83.6	1.85
A20	0.26	77.5	1.13

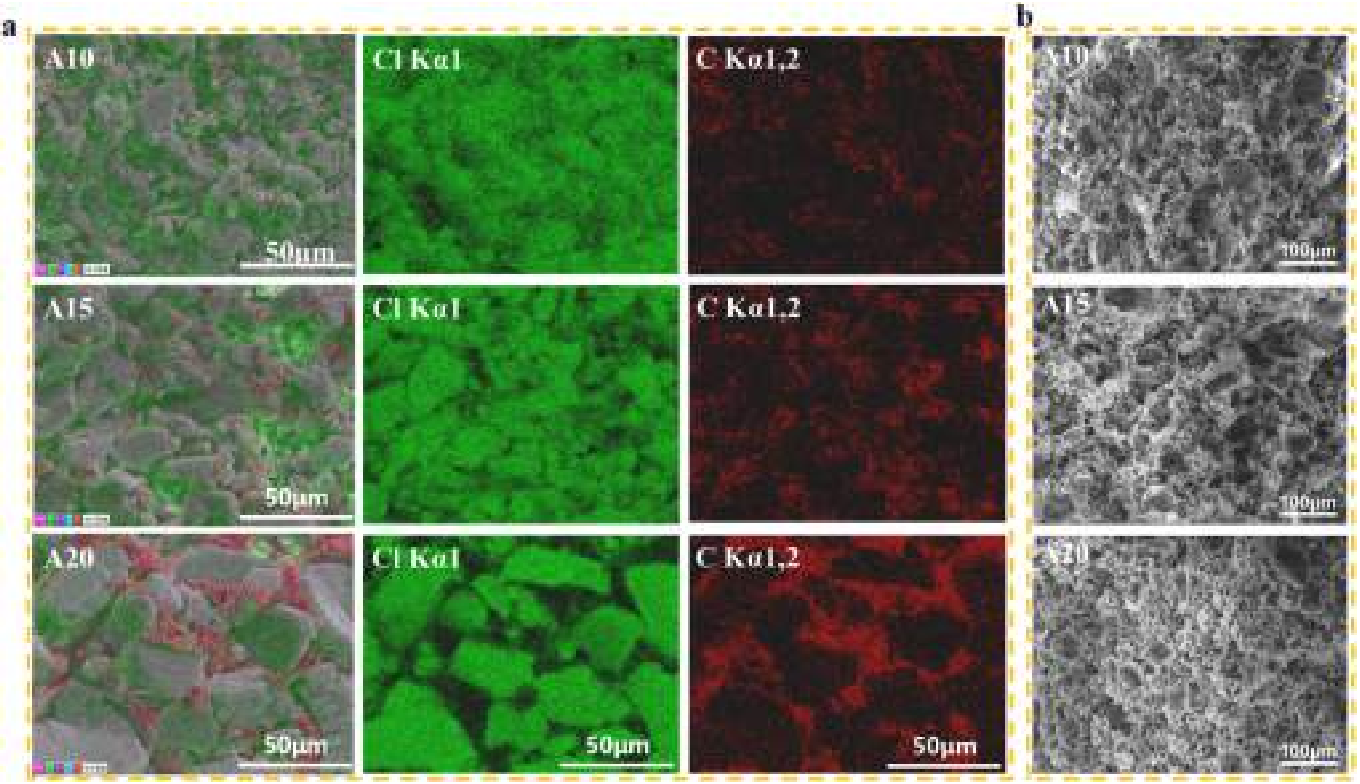

Fig. 2. a) EDS Mapping of the samples before removing the template. b) SEM images of the obtained SMPNA.

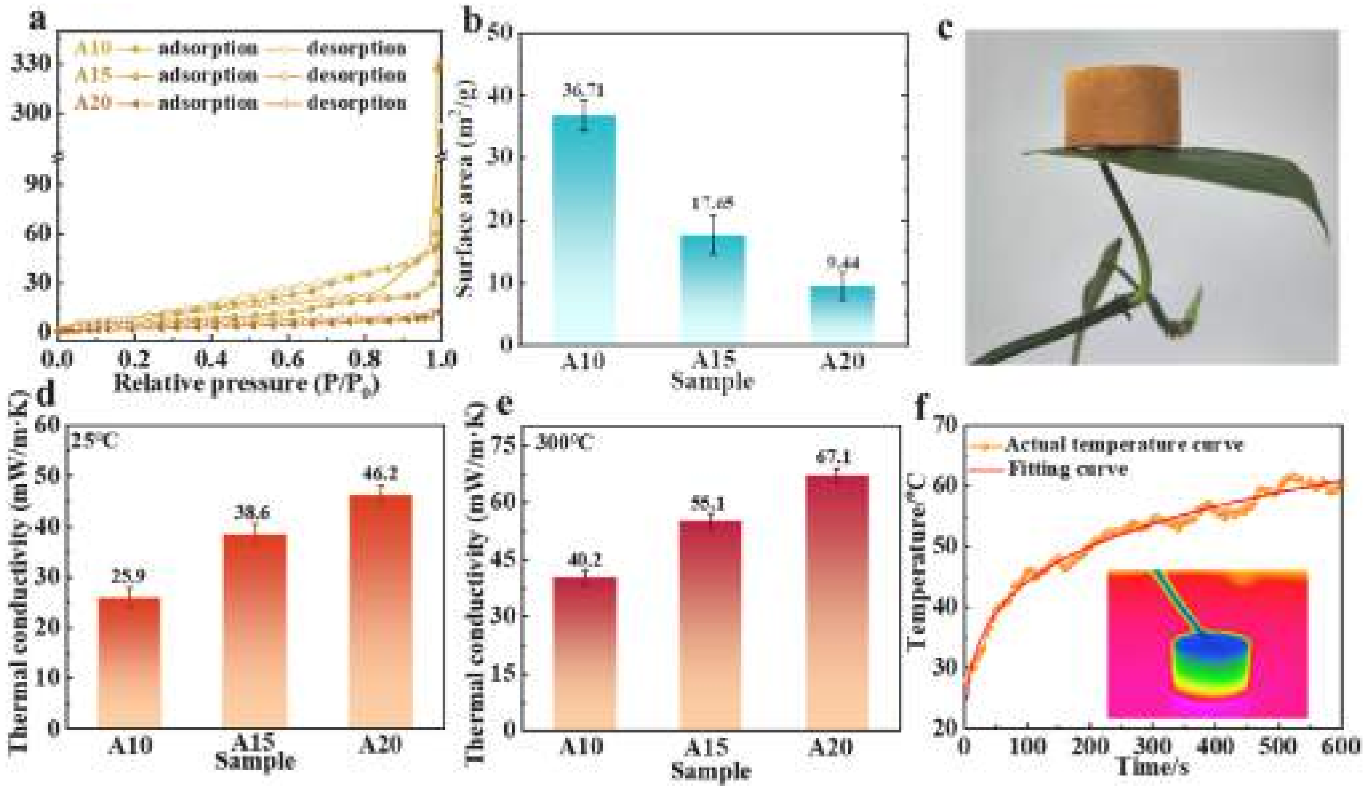

Fig. 3. a) N_2 adsorption-desorption isotherms and b) the specific surface area of SMPNA. c) Photograph of an ultralight A15 standing on top of a leaf. Thermal conductivity of the SMPNA at d) room temperature and e) 300 °C. f) Time-dependent temperature profile of A15 on the 300 °C heating panel, the inset image is the infrared thermal image.

the enhancement of overall strength within aerogel materials. The pore structure of the aerogel prepared via in situ polymerization template method is irregular due to the inherently disordered arrangement within the templates. The complex microporous morphology inside SMPNAs significantly enhance their ability to hinder heat conduction. Moreover, the disordered pore structure can provide a more uniform stress distribution under certain conditions, effectively reducing the local stress concentration and enabling the material to withstand greater pressure.

3.2. Surface properties and thermal insulating perfoemance

The specific surface area of the SMPN aerogel was examined through N_2 adsorption-desorption isotherms using the BET method. As shown in Fig. 3a, the aerogel displays the characteristics of a type III isotherm, and the adsorption capacity increases slowly with increasing relative pressure without any obvious adsorption saturation plateau, which can be attributed to the weak interaction between the material and nitrogen. The rise in the adsorption curve at the high-pressure region is mainly due to the uneven size of the micropore structure in the aerogel. The smaller the resin matrix content, the larger the volume occupied by the template, which means that the aerogel has a richer microporous structure after template removal, resulting in greater nitrogen adsorption capacity. Compared to A10 and A15, the adsorption isotherm curve of A20 displays gentler slopes due to its tighter pore structure. As shown in Fig. 3b, the specific surface areas of A10, A15 and A20 are calculated as approximately 36.71 m^2/g, 17.65 m^2/g and 9.44 m^2/g, respectively. Although the dense pore structure leads to a relatively low specific surface area, its comparatively high porosity, as listed in Table 2, ensures that the SMPNAs retain lightweight characteristics. Fig. 3c shows a cylindrical A15 sample with a diameter of 25 mm and a height of 20 mm supported by a leaf, demonstrating the lightweight property inherent to the SMPNA.

The thermal insulation performance represents a key application of aerogel materials, and the thermal conductivity of the SMPNA was assessed via a hot disk thermal conductivity analyser. Fig. 3d and e give the thermal conductivity values of the SMPNAs at room temperature and 300 °C, respectively. A high content template within the aerogel results in a more intricate pore structure, which effectively impedes heat conduction. The thermal conductivity of A20 is about 46.2 mW/m·K at room temperature, and then decreases to approximately 38.6 mW/m·K for A15, and 25.9 mW/m·K for A10. All of the aerogels exhibit low thermal conductivity at room temperature. Upon increasing the test temperature to 300 °C, the thermal conductivity exhibits an increase of nearly 50 %. Specifically, A10 demonstrates a value of approximately 40.2 mW/m·K, whereas A15 and A20 reach about 55.1 mW/m·K and 67.1 mW/m·K, respectively. The thermal conductivity remains relatively low at 300 °C, indicating that SMPNA possess good thermal insulation performance at high temperatures. To assess the thermal

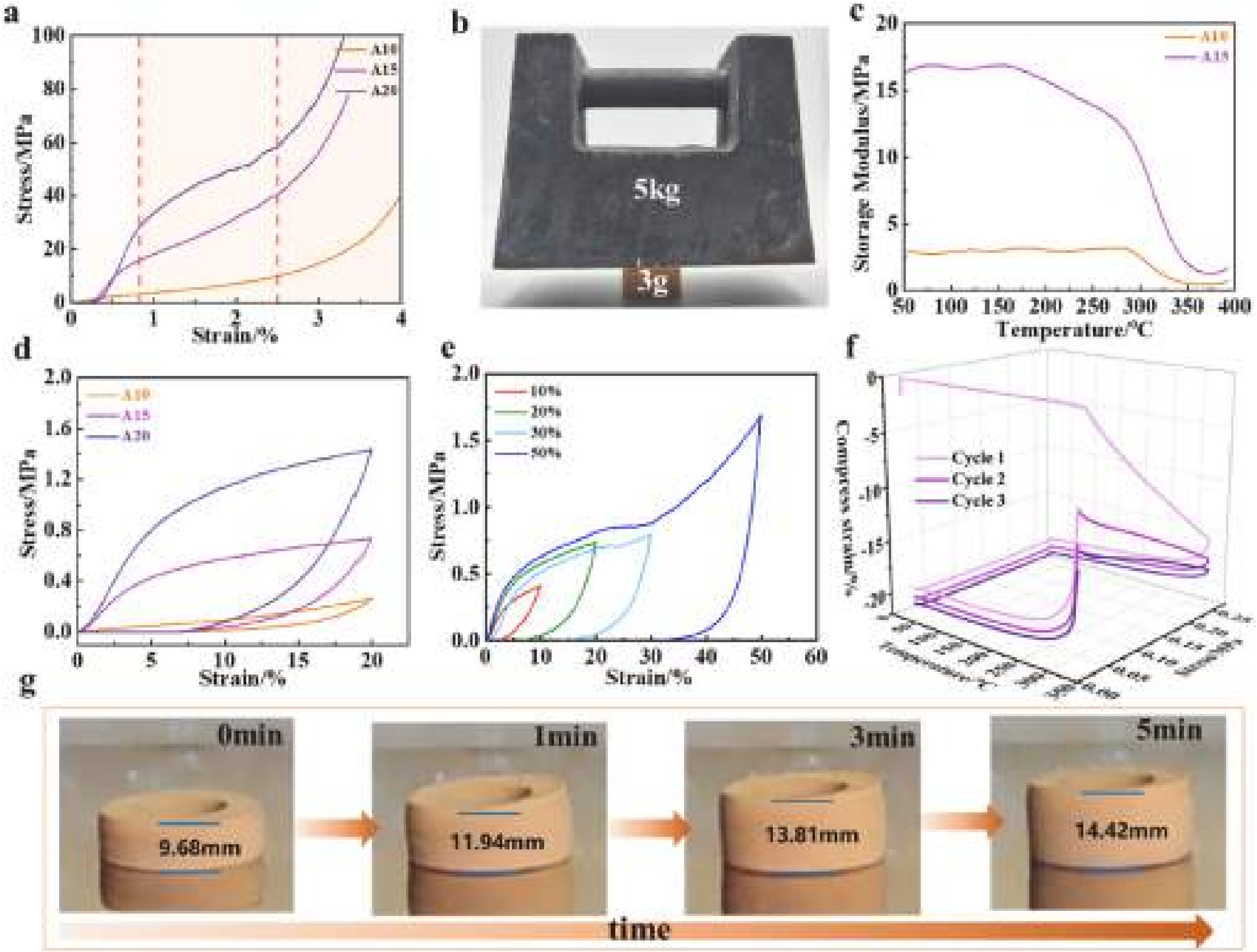

Fig. 4. a) Compression curves of SMPNAs at room temperature. b) Digital photo of A15 bear a weight. c) DMA curves of SMPNAs. d) Compression curves of SMPNAs at 350 °C with a compressive strain of 20 %. e) Compression curves of A15 at 350 °C with different compressive strain. f) Shape memory recycling curves of A15. g) Shape recovery process of SMPNA.

insulation of the SMPNA, an 18 mm thick cylindrical sample of A15 was placed on a heating table at 300 °C, and the surface temperature of the aerogel was monitored using a thermocouple. Fig. 3f gives the time-dependent temperature profile, with an inset displaying the infrared thermography image. The surface temperature rapidly increases to approximately 45 °C within 100 s and subsequently increases at a slower rate, stabilizing at around 60 °C after 600 s. The temperature differential between the upper and lower surfaces reaches 240 °C, demonstrating the exceptional insulation capabilities of SMPNA. This remarkable performance can be primarily attributed to the abundance of microscale pores present within the aerogel structure, which impedes the free movement of gas molecules and consequently reduces the thermal conductivity.

3.3. *Mechanical and shape memory effect*

Mechanical properties serve as crucial indicators for determining the applicability of materials. The compression properties of the SMPNAs were tested by electromechanical universal testing machines. Fig. 4a shows the compression stress-strain curve of the aerogel at room temperature. A10 exhibits poor mechanical strength, as its compression curve demonstrates a direct elastic-plastic behavior before the densification stage, which can be attributed to its loose pore structure and relatively thin pore walls. An increase in the matrix content results in enhanced mechanical strength of the aerogel, and the compression curves of A15 and A20 exhibit an almost linear relationship before the elastic-plastic stages, indicating the elastic behavior of the SMPNA. The elastic-plastic stress threshold of A15 is around 10 MPa, and that of A20 exceeds 20 MPa, suggesting a robust bearing capacity. Fig. 4b shows a weight of 5 kg pressed on the sample A15, with a diameter of 30 mm and an approximate mass of 3 g, demonstrating the high specific strength of SMPNA.

The dynamic mechanical properties of the SMPNAs were evaluated in compression mode using a DMA Q800. Fig. 4c illustrates the temperature-dependent storage modulus curves of A10 and A15, while the curve of A20 could not be obtained because the compressive stress surpasses the limit of the instrument. The strength of the aerogel is significantly enhanced with increasing matrix content. At room temperature, the storage modulus of A10 is about 2.5 MPa, whereas that of A15 reaches up to 17 MPa. In addition, the SMPN matrix endows the aerogels with variable stiffness characteristics, exhibiting a deformation temperature of around 330 °C. The storage modulus at 350 °C for A10 and A15 is approximately 0.5 MPa and 1.7 MPa, respectively. Fig. 4d shows the compression stress-strain curve of the aerogel at 350 °C. All the samples exhibit elastic recovery behavior at a compressive strain of 20 %, and the SMPNAs with higher SMPN matrix contents display larger compression modulus at high temperatures. Fig. 4e shows compression curves of A15 across various strain levels at 350 °C. The SMPNAs demonstrate satisfactory elastic recovery behavior until the compressive strain exceeds 30 %, and the sample with a compressive strain of 50 % recovers only approximately 20 % of the strain.

Significant compression of the aerogel can compromise its microporous structure, leading to irreversible partial strains. Shape memory cycling tests were conducted on A15 in compression mode, and the corresponding shape memory curve is shown in Fig. 4f. The shape fixing ratios for the first and second cycles are approximately 97.8 %, and the shape recovery rates are around 65 % and 75 %, respectively. The relatively low shape recovery rate of the aerogel can be attributed to its low thermal insulation, which impedes internal heating and subsequently delays shape recovery within a limited time. To better demonstrate the shape memory performance of the SMPNA, an A15 circular ring with a height of 16 mm was compressed to a thickness of 9.68 mm to establish a temporary shape. The shape recovery process occurred in an oven at 350 °C. Fig. 4g presents the intermediate transition shapes during the recovery process. The aerogel exhibits a slow shape recovery due to its low internal thermal insulation. It recovered to 14.42 mm after 5 min, with a shape recovery ratio of up to 90 %, indicating the excellent shape memory performance of SMPNA.

3.4. *Shape-controlled thermal insulation performance*

Based on its shape memory property, the SMPNA can be compressed and fixed into a temporary shape with a predetermined height. As illustrated in Fig. 5a, the initial sample height of 20 mm was adjusted to fixed heights of 16 mm and 12 mm, and the corresponding microstructures under different strains were characterized using SEM. At a strain of 20 %, the pores in the temporary shape become noticeably closer together. When the compression strain reaches 40 %, the micropore structure becomes significantly denser, with no large pores observed. The specific pore size distributions of SMPNA with different temporary shapes were analyzed by mercury porosimeter. As shown in Fig. 5b, the pore sizes of all the samples are concentrated within the range of 0.1–10 μm. With increased compression levels, the pore width decreases noticeably. According to Fig. 5c, the average pore diameter of the uncompressed aerogel is approximately 1.2 μm, which decreases to about 0.98 μm and 0.63 μm at strains of 20 % and 40 %, respectively. The variation in pore size will affect the thermal conductivity of the aerogel, and the specific impact is shown in Fig. 5d. In comparison to the original SMPNA, the thermal conductivity of the temporary SMPNA with 20 % compression exhibits a slight increase to 39.40 mW/m·K. This increase can be attributed to limited compression on the pores, which still maintains an effective barrier against heat transfer. When subjected to a fixed strain of 40 %, there is a notable increase in the thermal conductivity of SMPNAs, reaching up to 46.64 mW/m·K, which results from the reduced thermal conduction distance caused by the compressed micropore structure.

Samples with temporary shapes of different heights were placed on a heating stage to evaluate their heat-shielding performance. Fig. 5e presents the thermal infrared images captured at different heating temperatures. After 600 s of exposure to a temperature of 100 °C, the surface temperature of the original SMPNA, the samples with fixed strains of 20 % and 40 % were approximately 34 °C, 38 °C, and 41 °C. When exposed to 200 °C for 600 s, the surface temperature of the original SMPNA is approximately 53 °C, while those of the samples with 20 % and 40 % fixed strains are approximately 64 °C and 70 °C, respectively. As the heating temperature increases, the heat-shielding performance of SMPNAs with different fixed strains becomes more pronounced. At a heating stage temperature of 300 °C, the surface temperature of the uncompressed SMPNA rises to 69 °C, while the samples under fixed strains of 20 % and 40 % reach 82 °C and 91 °C, respectively. These results indicate that SMPNAs possess tunable thermal conductivity through their shape memory performance. In a low-temperature environment, a thinner SMPNA with a compressed temporary shape can provide effective heat-shielding performance. In high-temperature environments, the heat-shielding performance of SMPNA can be enhanced by modifying its micropore structure through the shape recovery process.

Owing to their exceptional thermal insulation properties, SMPNAs exhibit significant potential for application in the field of infrared stealth materials. As shown in Fig. 5f, when a circular SMPNA ring with a thickness of 6 mm was placed on an iron rod heated to approximately 120 °C, the ring initially blends seamlessly into the surrounding infrared environment, achieving effective camouflage. After 60 s, although there is a slight increase in the temperature of the ring, it maintains excellent environmental adaptation, indicating its potential use in infrared stealth applications. Additionally, the thickness of the SMPNA can be precisely modified owing to its unique shape memory characteristics, which enables further optimization of its infrared stealth properties. Fig. 5g shows that a 5 mm-thick SMPNA was fixed to a 3 mm temporary shape and then placed on the surface of an aircraft model heated to 100 °C. After 60 s, the temperature of the original SMPNA was around 40 °C, maintaining a stealth state, while the compressed temporary shape sample reached 60 °C, exiting the stealth state. This selective infrared

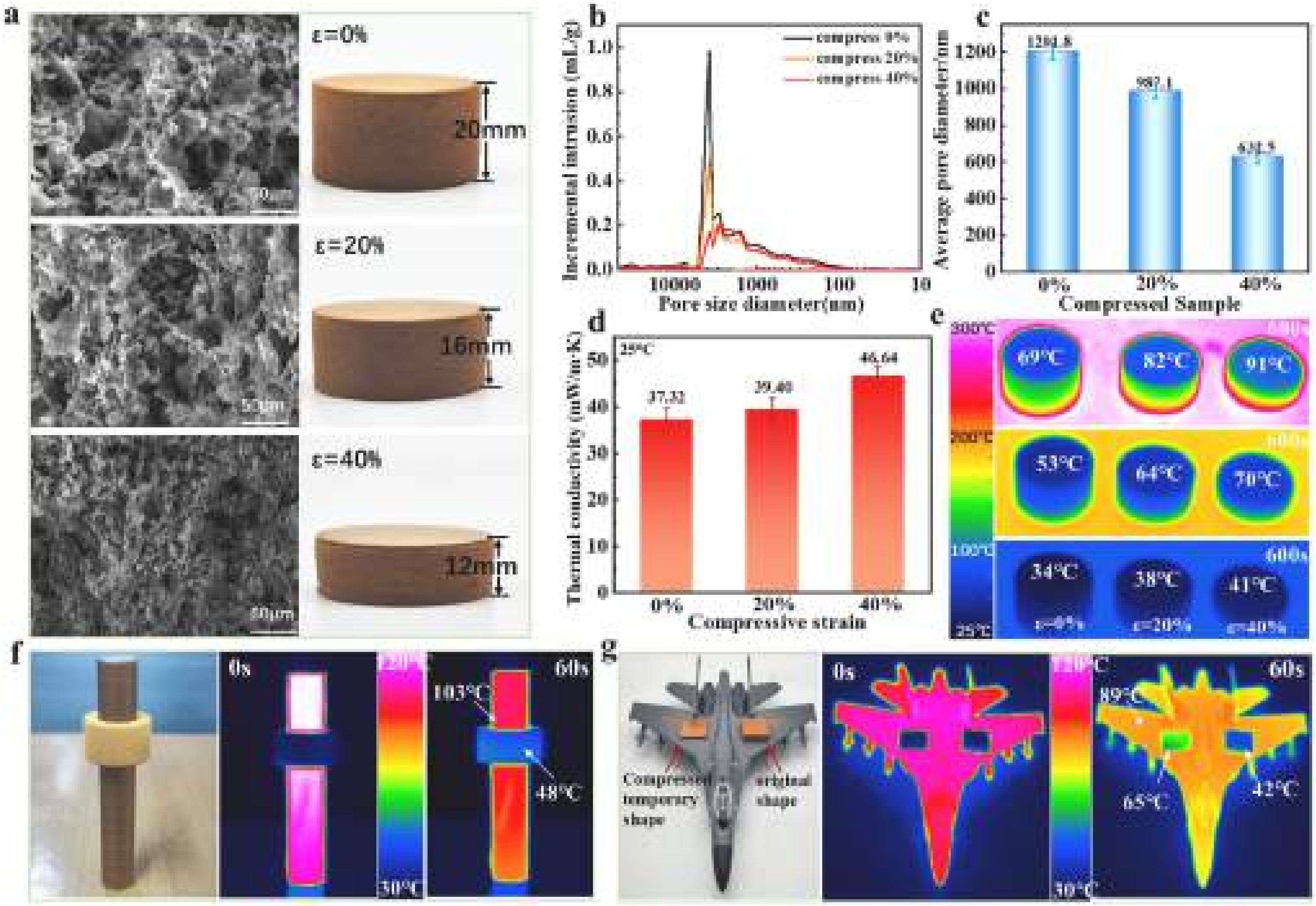

Fig. 5. a) SEM images and digital photo of the SMPNA with different compressed temporary shape. b) Pore distribution, c) average pore diameter, and d) thermal conductivity of the SMPNA with different compressed temporary shape. e) Thermal infrared image of the samples in the heating stage; f) Demonstration of SMPNA for infrared stealth. g) Adjustable infrared stealth performance of SMPNA.

stealth capability allows SMPNAs to adjust their environmental compatibility through shape memory, enabling controlled stealth or exposure based on specific requirements.

3.5. Dynamic thermal protection

The thermal stability of the SMPNAs was evaluated by TGA. As illustrated in Fig. 6a, the SMPNA demonstrates exceptional thermal stability, with a 5 % decomposition temperature (T_{d5}) above 421 °C and a residual carbon yield at 1000 °C (C_{y1000}) exceeding 42 %. The T_{d5} of SMPNA is slightly lower than that of SMPN [22]. This can be attributed to its porous structure facilitating the escape of decomposed small molecules. The thermal protection performance of the SMPNA with a height of 20 mm was tested using a butane flame, and the process was recorded using an infrared camera, as shown in Supporting Video 1. Fig. 6b and c shows the thermal infrared images and the temperature variations on the front and back surfaces of the SMPNA. The front surface temperature increases rapidly to around 800 °C before stabilizing, while the back surface experiences a more gradual rise, reaching approximately 100 °C within 200 s. This indicates that SMPNA possesses excellent thermal insulation performance against flames, suggesting its potential application in harsh high-temperature environments. When the SMPNA is fixed into a compressed temporary shape (Fig. 6d), its inherent shape memory property allows it to expand through micropores and recover to its original shape, thereby regulating its thermal insulation properties under high-temperature flames. The specific recovery process can be observed in Supporting Videos 2 and 3. Fig. 6e illustrates the dynamic thermal insulation mechanism of SMPNA. The abundant microporous structure within SMPNA is filled with air, which restricts the movement of gas molecules that transport heat, thereby limiting both thermal conduction and convection. Additionally, the abundant microporous structure features complex pore walls that facilitate heat conduction, increasing the distance for thermal flux and effectively dissipating thermal energy. When SMPNA is fixed into compressed temporary shape, its microporous structure becomes more compact, resulting in an increase in thermal conductivity. Upon exposure to a high-temperature environment, the absorbed thermal energy drives the compressed structure to recover and expand, leading to a decrease in thermal conductivity and an increase in heat-shielding performance.

3.6. Thermal dimensional stability and wave absorption after thermal treatment

To investigate the potential applications of SMPNA in high-temperature environments, the sample A15 with a diameter of 26 mm was placed in a tubular furnace and annealed for 1 h at 400 °C, 600 °C, 800 °C, 1000 °C and 1200 °C. The thermally treated samples were labeled as T400, T600, T800, T1000, and T1200. Fig. 7a shows the linear shrinkage rates of the SMPNAs treated at various temperatures, along with photographs of the samples after thermal treatment. The results indicate that the shrinkage rate for the sample T400 is only 0.34 %, demonstrating excellent thermal stability and potential for long-term and stable service in environments below 400 °C. As the treatment

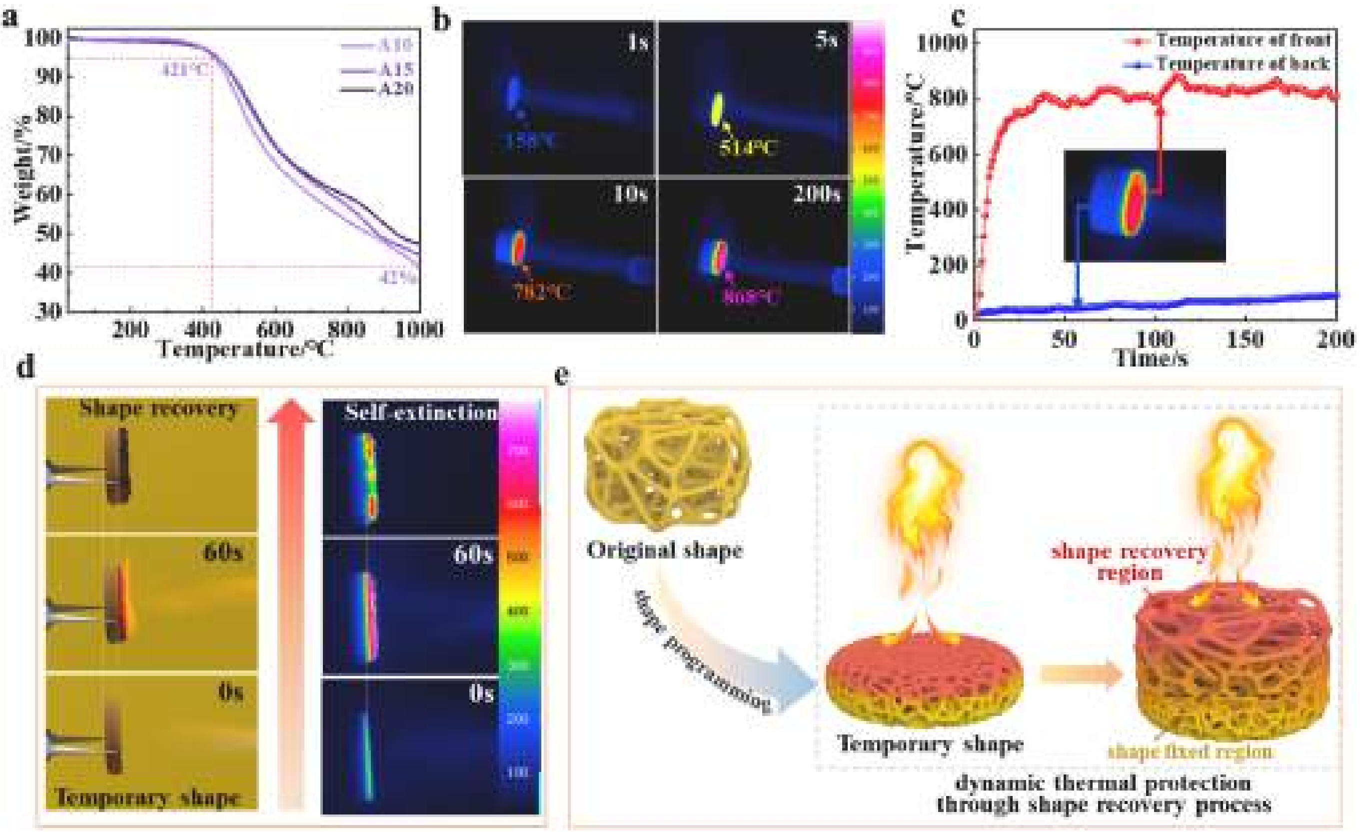

Fig. 6. a) TGA curves of SMPNA. b) Infrared images of the thermal protection of SMPNA against butane flame. c) Temperature variations on the front and back surface of SMPNA. d) Dynamic thermal protection of the SMPNA with fixed temporary shape. e) Thermal protection mechanism of the SMPNA against high temperature.

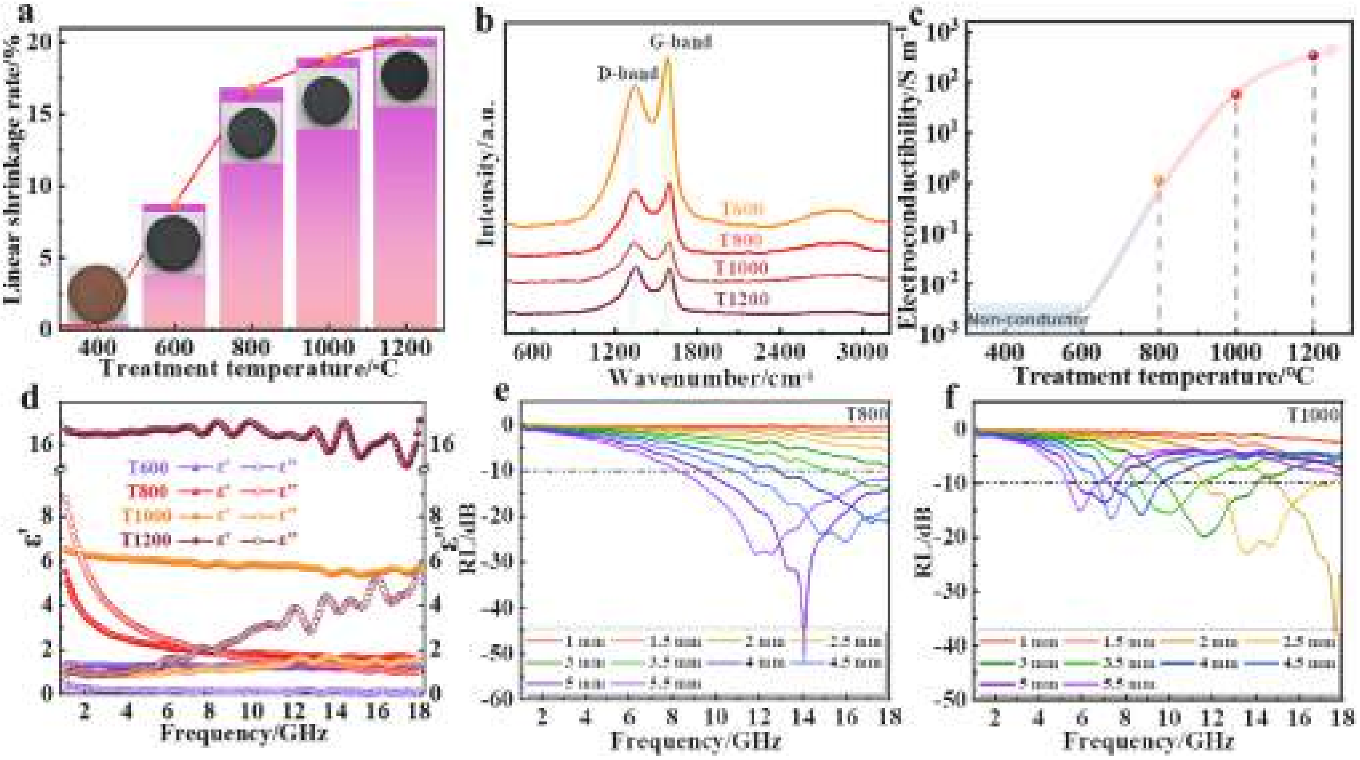

Fig. 7. a) Linear shrinkage rate of the thermally-treated SMPNAs. b) Raman spectrum of the SMPNA annealed at different temperature. c) Conductivity variation of the SMPNA treated at different temperature. d) Frequency-dependent permittivity curves of the thermally-treated SMPNAs. Reflection loss curves of e) T800 and f) T1000.

temperature increases, the SMPNAs begin to shrink. The linear shrinkage of T600 reaches 8.72 %, while it further increases to 16.8 % for T800. Notably, the dimensional shrinkage rate gradually decelerates above 800 °C, with linear shrinkage rates of 18.8 % and 20.2 % for samples T1000 and T1200, respectively. The shrinkage rate of SMPNA at 1000 °C remains below 20 %, indicating excellent thermal dimensional stability that significantly surpasses that of organic aerogels [23–25], which can be attributed to a stable carbon skeleton with abundant benzene rings in the SMPNA matrix. The micromorphology of the treated samples was investigated by SEM. As shown in Fig. S4, there was no significant difference in the micromorphology between T400 and untreated SMPNAs. The microporous structure of T600 exhibits a certain shrinkage, which becomes more pronounced with increasing the treatment temperature. In addition, the micropore collapse rarely occurs in SMPNAs during thermal decomposition. The SMPNAs primarily undergo skeleton shrinkage, enabling them to preserve their porous morphology and exhibit excellent thermal dimensional stability.

The chemical structure of the thermally treated SMPNAs was investigated through Raman spectroscopy. As illustrated in Fig. 7b, that T600 exhibits a D-band absorption peak at 1350 cm^{-1}, representing graphite structural defects, and a G-band absorption peak at 1580 cm^{-1}, which corresponds to the sp^2 C–C bonding structure with integrity graphite [26]. Since 600 °C is far below the typical graphitization temperature (usually above 2000 °C), the prominent G peak is primarily attributed to the disordered sp^2 carbon structure generated during the carbonization of the aromatic-rich matrix. As the treatment temperature increases, a gradual decrease in relative intensity of the G peak is observed in the Raman spectra of samples T800, T1000, and T1200. And the relative intensity of the D peak increases correspondingly, indicating that higher decomposition temperatures promote the formation of more irregular hybrid of sp^2carbon structures and defect-rich graphite-like carbon. These defects are primarily introduced by the heteroatoms such as oxygen and nitrogen in the matrix, which disrupt the hybrid conjugated region [27]. The bulk resistance of the thermally treated SMPNAs was measured using a four-point probe, and the corresponding conductivity was calculated. Fig. 7c shows the relationship between the annealing temperature and conductivity. Although the SMPNA begins to undergo carbonize at 600 °C, the conductivity of T600 cannot be calculated due to its excessively high resistance caused by the low degree of carbonization at this temperature. As the annealing temperature increases, a greater portion of the SMPN matrix is converted into graphite-like structures, and the conductivity of T800 rises to approximately 1 S/m. Furthermore, the conductivity of T1000 nearly approaches 10^2 S/m, indicating substantial electrical conductivity. When the treatment temperature reaches 1200 °C, the conductivity of the sample increased to approximately 500 S/m at a slower rate.

The conductivity of a material significantly influences its dielectric property, which further influence its electromagnetic behavior [28]. The microwave absorption properties of the thermally treated SMPNAs were investigated with a coaxial method using a Vector Network Analyzer. Fig. 7d shows the frequency-dependent permittivity curves of the annealed samples. In T600, both the real part (ε') and the imaginary part (ε'') of the dielectric constant exhibit relatively low values across the entire tested frequency range, which represent the polarization capacity for impedance matching and the microwave loss capability, respectively. The low ε' of T600 indicates a weak polarization response to the electric field, allowing microwaves to easily penetrate the material. And the low ε'' suggests that T600 has limited dielectric loss, reflecting an inadequate capacity to dissipate electromagnetic energy [29]. The frequency-dependent reflection loss (RL) curves of the thermally treated SMPNAs were derived using transmission line theory, and the RL value serves as an indicator of the absorptive capacity of materials. The RL below −10 dB indicating that more than 90 % of the incident microwaves are absorbed and attenuated [30]. As shown in Fig. S5a, the RL of T600 remains above −10 dB across all the tested frequency ranges, indicating its inability to absorb microwaves. The ε' and ε'' of T800 decrease gradually from low frequency to high frequency, demonstrating typical frequency dispersion behavior, which is beneficial for achieving broadband microwave absorption [31]. The conductive network of T800 remains not fully continuous due to its lower conductivity compared to that of T1000 and T1200. This discontinuous conductive structure results in electron hopping between isolated conductive islands, thereby inducing significant conduction losses. Furthermore, the presence of interfacial defects within the graphite-like carbon structure of T800, as evidenced by Raman spectra, contributed to conduction loss through interfacial and dipolar polarization, which results in higher ε'' value than ε' value in the low-frequency range [32]. As shown in Fig. 7e, T800 demonstrates effective microwave absorption capabilities at certain frequencies when its thickness exceeds 3 mm. Notably, at a thickness of 5.5 mm, the effective absorption bandwidth of T800 reaches up to 10 GHz and spans from 8 to 18 GHz, making it advantageous for applications within a multifrequency band environment. As the treatment temperature increases, a more continuous conductive network is established in T1000. Fig. 7d shows that the ε' of T1000 increases significantly, reflecting an enhanced polarization response to the electric field. And the ε'' becomes more stable across the frequency range, suggesting that the electron transport mechanism has shifted from localized hopping between isolated conductive regions to long-range conduction along continuous pathways [32]. Fig. 7f reveals that T1000 displays excellent wave absorption performance within specific frequency bands once its thickness surpasses 1.5 mm. However, as the thickness further increases, the frequency range for absorbing microwaves gradually narrows, while the absorption efficiency decreases. As the treatment temperature increases further, Fig. 7d shows that the ε'' of T1200 increases with frequency, meaning an improvement in the loss capacity at high frequency. However, an excessively high ε' can lead to impedance mismatch, causing strong reflection of incident microwave. Fig. S5b shows that T1200 is unable to absorb microwaves effectively. The microwave absorption properties of annealed SMPNA are primarily influenced by the treatment temperature, which determines the degree of carbonization. After thermal treatment, the retained complex porous structure of T800 facilitates multiple internal pathways for both the reflection and scattering of microwaves, thereby enhancing wave loss and achieving superior wave absorption performance over a wide frequency range. The wave-absorbing properties could expand potential applications for SMPNAs within high-temperature environments.

3.7. Carbon nanotubes composite SMPNA

To further expand the application of SMPNA in microwave absorption, multi-walled carbon nanotubes (MWCNTs) were incorporated as functional additives during the mixing process of the NaCl template and SMPNA prepolymer, with MWCNTs contents of 2 %, 5 %, 8 %, and 10 % by weight of the polymer matrix. Fig. S6 shows the microstructure of the SMPNA composite (SMPNAc) with different MWCNTs contents. The MWCNTs exhibit good interfacial compatibility with the resin matrix, as they are almost integrated with the pore wall. Fig. S7 shows the thermal conductivity of SMPNAc as a function of MWCNTs contents. A small addition of MWCNTs can markedly enhance the thermal conductivity of SMPNAc due to its low phonon scattering and high thermal conductivity originated from unique one-dimensional structure and strong C–C bonds of carbon nanotubes. The SMPNAc with 2 % MWCNTs reaches 48.9 mW/m·K, while that with 10 % MWCNTs exceeds 100 mW/m·K.

Owing to the unique electron transport properties of carbon nanotubes, the incorporation of MWCNTs led to a more pronounced change in conductivity. Fig. 8a illustrates the variation in conductivity of the resulting SMPNAc as a function of MWCNT contents. When the MWCNT content reaches 2 %, the electrical conductivity of SMPNAc reaches 7.9×10^{-5} S/m and continues to increase with increasing MWCNTs contents. The SMPNAc with 8 % MWCNTs exhibits a conductivity of 0.508 S/m, after which the improvement slows down. The dielectric properties

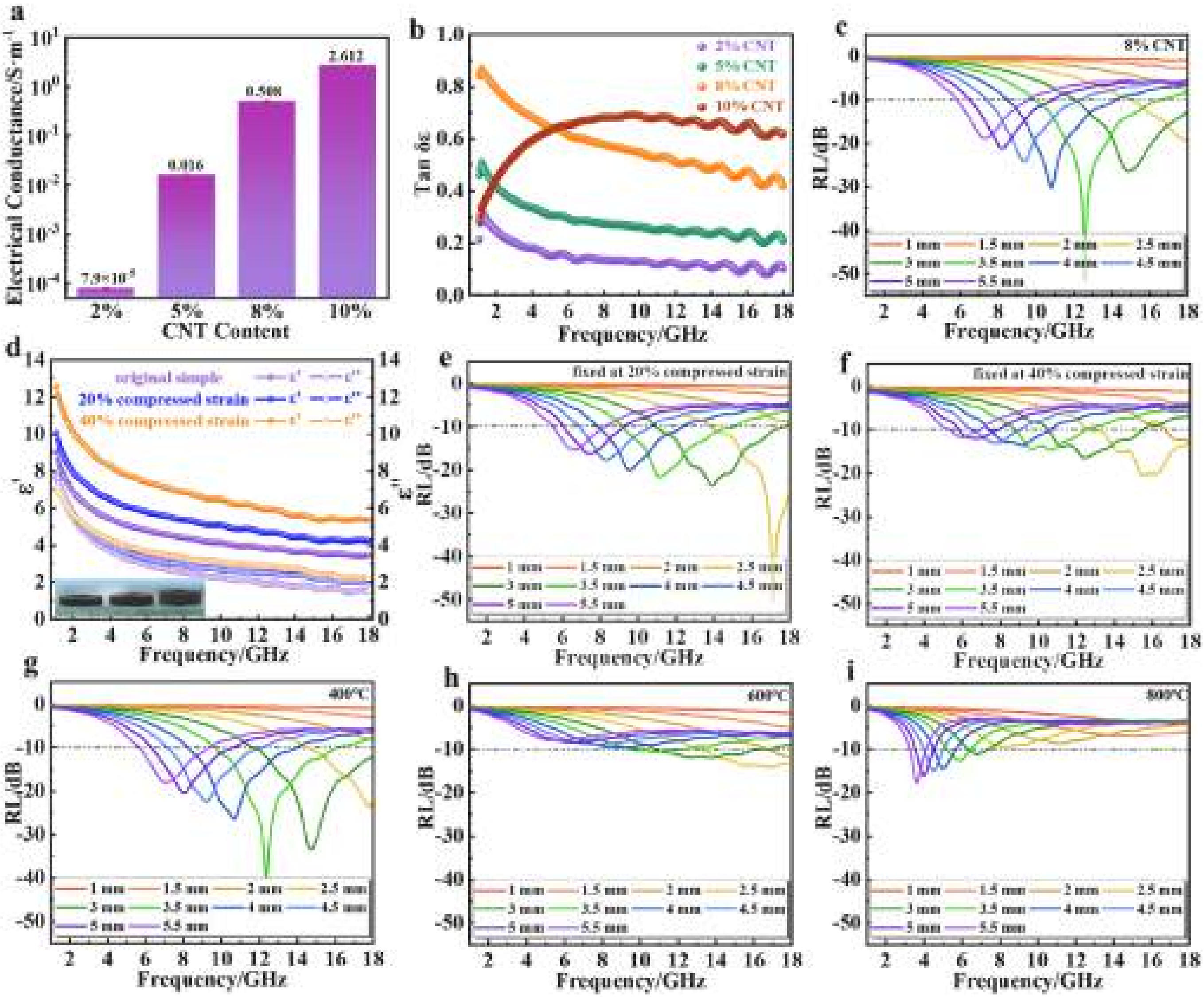

Fig. 8. a) Conductivity and b) dielectric loss tangents curves of SMPNAc. c) Frequency-dependent reflection losses of SMPNAc contained 8 % MWCNTs. d) Permittivity parameters versus frequency of SMPNAc fixed at different compressed strains. Frequency-dependent reflection losses of SMPNAc fixed at e) 20 % and f) 40 % compressed strain. Frequency-dependent reflection losses of SMPNAc after thermal treatment at g) 400 °C, h) 600 °C and i) 800 °C.

of SMPNAc were extensively investigated using a Vector Network Analyzer with the coaxial method, the frequency-dependent permittivity curves of SMPNAc are shown in Fig. S8, and the dielectric loss tangents ($\tan\delta_\varepsilon = \varepsilon''/\varepsilon'$) curves are presented in Fig. 8b. As the MWCNTs content increases, both the ε' and the ε'' of SMPNAc increase significantly, especially in the low-frequency range. This enhancement is primarily attributed to the gradual formation of a conductive network by the MWCNT within the matrix, as well as the synergistic effects of interfacial polarization and conduction loss [29]. The $\tan\delta_\varepsilon$ of the SMPNAc containing approximately 2 % and 5 % MWCNTs remains relatively low across the tested frequency range, indicating a limited contribution to microwave attenuation. The SMPNAc containing 8 % MWCNTs exhibits a comparatively high $\tan\delta_\varepsilon$ (approximately 0.9–0.5) across the entire frequency band, suggesting that the established conductive network facilitates considerable dielectric loss and promotes efficientive dissipation of incident microwave energy. The RL curves of SMPNAc were fitted based on transmission line theory. As shown in Fig. S9, although the SMPNAc with 5 % MWCNTs demonstrates superior microwave absorption capacity compared to those enhanced with 2 % MWCNTs, its RL remains above −10 dB, indicating weak microwave absorption, which is consistent with the conclusion from the $\tan\delta_\varepsilon$ curves. Fig. 8c shows that SMPNAc with 8 % MWCNTs presents effective wave absorption at high frequency when its thickness exceeds 2.5 mm, which can be attributed to favorable impedance matching and efficient microwave energy dissipation. As the MWCNT content further increases, it can be seen from Fig. 8b that the $\tan\delta_\varepsilon$ of the SMPNAc with 10 % MWCNT increases with frequency, exhibiting a trend opposite to that of SMPNAc with lower MWCNTs content. This alteration is primarily due to the formation of a continuous conductive network that facilitates the migration of free carriers, thereby enhancing dielectric loss and energy dissipation at the low frequencies [32]. Although a higher ε'' promotes the dissipation of incident microwaves, a significant increase in ε' results in impedance mismatch, which heightens the reflection of incident microwaves and ultimately diminishes the overall absorption performance. The optimization of the microwave absorption performance relies not solely on the magnitude of the dielectric constant, but also the balance of the dielectric loss and impedance matching. The RL curves presented in Fig. S9c indicate that SMPNAc with 10 % MWCNT content compromises the microwave absorption performance. Fig. S9d shows the RL curves for various MWCNT contents at a thickness of 3 mm, revealing the optimal performance for the SMPNAc containing 8 % MWCNTs.

The SMPNAc can be fixed at different thicknesses through variable stiffness due to its shape memory property. The inset image in Fig. 8d illustrates the fixed states of the SMPNAc containing 8 % MWCNTs under different compression thicknesses, and Fig. 8d presents the frequency-dependent permittivity curves of the SMPNAc at the corresponding fixed thickness. As the compressive strain increases, the reduction in the spacing between MWCNTs results in a denser conductive network, enhanced polarization and increased conduction loss, thereby amplifying the ε' and ε″ [33]. However, a substantial increase in ε' will alter the polarization capacity of SMPNAc, disrupting the balance between permittivity and permeability in the material and leading to impedance mismatch. Fig. 8e shows that SMPNAc with a temporary shape fixed at a compressed strain of 20 % still exhibits a decent wave absorption, but the optimal absorption thickness changes from the original 3.5 mm–2.5 mm, closely matching the compression ratio. When the compressed strain increases to 40 %, there is a marked decrease in wave absorption capacity. The optimal absorption thickness remains at 2.5 mm, but its RL intensity decreases. According to the permittivity curves (Fig. 8d), this can be attributed to impedance mismatch caused by the significant increase in ε', which hinders the penetration of microwaves.

In order to investigate the applicable temperature of the microwave absorbing properties, the SMPNAc containing 8 % MWCNTs was thermally treated at 400 °C, 600 °C, 800 °C, and 1000 °C in nitrogen atmospheres for study. Fig. S10 illustrates the frequency-dependent permittivity curves and $\tan\delta_\varepsilon$ curves. These results indicate that as the treatment temperature increases, the carbonization of the SMPNA matrix significantly influences the dielectric properties of SMPNAc. Although elevated temperatures enhance the ε'' parameter and facilitate microwave energy dissipation, it ε' parameter is also altered, leading to impedance mismatch and an increase of the incident microwaves reflection. As shown in Fig. 8g, the SMPNAc treated at 400 °C retains decent microwave absorbing property with the ε' and ε'' values comparable to those of untreated sample (Fig. S10a), which can be attributed to the stable structure below 400 °C. In contrast, the SMPNAc treated at 600 °C is only capable of absorbing microwaves within a certain high-frequency band at a specific thickness (Fig. 8h), mainly due to the impedance mismatch caused by the carbonization of the matrix. Fig. 8i shows that the SMPNAc treated at 800 °C cannot absorb microwaves in the high-frequency band. However, it demonstrates absorption capabilities in the low-frequency band, particularly as the thickness increases. This should be the result of the synergy between the carbonized matrix and MWCNTs, as the matrix treated at 800 °C possesses good wave-absorbing capacity, while MWCNTs alter the dielectric properties of SMPNAc. With the increase in treatment temperature, the further carbonization of the matrix enhances ε' and aggravates impedance mismatch, make it insufficient for effective microwave absorption (Fig. S11). Hence, the operating temperature of SMPNAc for stable microwave absorption is within 400 °C. Moreover, efficient microwave absorption within the low-frequency band can be achieved through thermal treatment at 800 °C.

4. Conclusion

In this work, reconfigurable high-temperature, thermally protected SMPNAs were developed through a facile in situ polymerization templating method. The resulting SMPNA exhibits isotropic microporous structures that enhance its compression resistance at room temperature. The SMPN matrix endows the SMPNA with shape memory properties, allowing it to be deformed and compressed at high temperature and fixed at room temperature. The SMPNA demonstrates low thermal conductivity below 50 mW/m·k before and after the deformation, indicating robust heat-shielding performance. Furthermore, the compressed and fixed SMPNA can provide dynamic thermal protection through gradual shape recovery at high temperatures. In addition, SMPNA still exhibits excellent thermal dimensional stability, with almost no shrinkage at 400 °C and only 18.8 % linear shrinkage rate at 1000 °C. In addition, the SMPNA thermally treated at 800 °C displays high microwave absorption performance across a wide frequency range from 8 GHz to 18 GHz, broadening the potential application of SMPNAs in high-temperature environments. Moreover, the SMPNAc incorporated with 8 % MWCNTs endows the composite with improved impedance matching and moderate dielectric loss. The highly thermally stable matrix ensures stable microwave absorption up to 400 °C, thereby fulfilling the requirements for microwave absorption in various applications.

CRediT authorship contribution statement

Rongxiang Hu: Writing – original draft, Methodology, Investigation. **Fenghua Zhang:** Writing – review & editing, Project administration, Funding acquisition. **Lan Luo:** Visualization, Formal analysis. **Linlin Wang:** Formal analysis, Data curation. **Yanju Liu:** Project administration, Funding acquisition. **Jinsong Leng:** Supervision, Conceptualization.

Declaration of competing interest

The authors declare that they have no known competing financial interests or personal

Relationships that could have appeared to influence the work reported in this paper.

Acknowledgements

This work was financially supported by the National Natural Science Foundation of China (Grant No. 92271112 and No.92271206).

Appendix A. Supplementary data

Supplementary data to this article can be found online at https://doi.org/10.1016/j.carbon.2025.120378.

References

[1] Y.K. Liu, L.L. Wang, Y.J. Liu, F.H. Zhang, J.S. Leng, Compos. Commun. 51 (2024) 102062, https://doi.org/10.1016/j.coco.2024.102062.

[2] C.J. Ni, D. Chen, Y. Yin, X. Wen, X.L. Chen, C. Yang, G.C. Chen, Z. Sun, J.H. Wen, Y. R. Jiao, C.Y. Wang, N. Wang, X.X. Kong, S.H. Deng, Y.Q. Shen, R. Xiao, X.M. Jin, J. Li, X.Q. Kong, Q. Zhao, T. Xie, Nature 622 (7984) (2023) 748–753, https://doi.org/10.1038/s41586-023-06520-8.

[3] E. Yarali, M. Baniasadi, A. Zolfagharian, M. Chavoshi, F. Arefi, M. Hossain, A. Bastola, M. Ansari, A. Foyouzat, A. Dabbagh, M. Ebrahimi, M.J. Mirzaali, M. Bodaghi, Appl. Mater. Today 26 (2022) 101306, https://doi.org/10.1016/j.apmt.2021.101306.

[4] L. Luo, F.H. Zhang, L.L. Wang, Y.J. Liu, J.S. Leng, Adv. Funct. Mater. 34 (14) (2024) 2312036, https://doi.org/10.1002/adfm.202312036.

[5] M.Y. Khalid, Z.U. Arif, A. Tariq, M. Hossain, K.A. Khan, R. Umer, Eur. Polym. J. 205 (2024) 112718, https://doi.org/10.1016/j.eurpolymj.2023.112718.

[6] T.W. Liu, J.B. Bai, N. Fantuzzi, X. Zhang, Prog. Aero. Sci. 146 (2024) 100985, https://doi.org/10.1016/j.paerosci.2024.100985.

[7] L. Luo, F. Zhang, J. Leng, Research 2022. https://doi.org/10.34133/2022/9767830, 2022.

[8] Q.W. Geng, F.H. Zhang, Y.J. Liu, J.S. Leng, Compos. Sci. Technol. 242 (2023) 110169, https://doi.org/10.1016/j.compscitech.2023.110169.

[9] Z.H. Li, Z.W. Li, S.H. Zhou, J.M. Zhang, L. Zong, Small 20 (25) (2024) 2311240, https://doi.org/10.1002/smll.202311240.

[10] Y. Yao, P.T. Hoang, T. Liu, J. Mater. Sci. Technol. 33 (8) (2017) 869–873, https://doi.org/10.1016/j.jmst.2016.05.017.

[11] Y. Bai, J. Zhang, D. Wen, P. Gong, J. Liu, J. Ju, X. Chen, Compos. Sci. Technol. 187 (2020) 107940, https://doi.org/10.1016/j.compscitech.2019.107940.

[12] Z.Z. Tang, G. Deng, P.R. Cao, J.H. Gong, J. Yang, Z.H. Yang, Y.Y. Sun, L.M. Tao, T. M. Wang, Q.H. Wang, Y.M. Zhang, ACS Appl. Mater. Interfaces 15 (20) (2023) 24968–24977, https://doi.org/10.1021/acsami.3c04620.

[13] J.H. Lee, S.J. Park, Carbon 163 (2020) 1–18, https://doi.org/10.1016/j.carbon.2020.02.073.

[14] S.S. Sonu, N. Rai, I. Chauhan, J. Sol. Gel Sci. Technol. 105 (2) (2023) 324–336, https://doi.org/10.1007/s10971-022-06026-1.

[15] L. Su, S.H. Jia, J.Q. Ren, X.F. Lu, S.W. Guo, P.F. Guo, Z.X. Cai, D. Lu, M. Niu, L. Zhuang, K. Peng, H.J. Wang, Nat. Commun. 14 (1) (2023) 7057, https://doi.org/10.1038/s41467-023-42703-7.

[16] Z.L. Yu, B. Qin, Z.Y. Ma, J. Huang, S.C. Li, H.Y. Zhao, H. Li, Y.B. Zhu, H.A. Wu, S. H. Yu, Adv. Mater. 31 (23) (2019), https://doi.org/10.1002/adma.201900651.

[17] B. Tian, X. Jiang, W. Chu, C. Zheng, W. Guo, Z. Zhang, Int J Smart Nano Mater 14 (2) (2023) 230–242, https://doi.org/10.1080/19475411.2023.2205176.

[18] J. Tian, Y. Yang, T. Xue, G. Chao, W. Fan, T. Liu, J. Mater. Sci. Technol. 105 (2022) 194–202, https://doi.org/10.1016/j.jmst.2021.07.030.

[19] X. Xiao, M. Panahi-Sarmad, R. Xu, A. Wang, S. Cao, K. Zhang, M. Kamkar, M. Noroozi, Eur. Polym. J. 179 (2022) 111531, https://doi.org/10.1016/j.eurpolymj.2022.111531.

[20] J.R. Wu, L.P. Zeng, X.P. Huang, L.J. Zhao, G.S. Huang, J. Mater. Chem. A 5 (29) (2017) 15048–15055, https://doi.org/10.1039/c7ta02686b.

[21] M.H. Guo, Y.F. Zhang, C. Huang, X. Zhao, X.P. Yan, Y.P. Huang, L. Li, T.X. Liu, COMPOS PART A-APPL S 174 (2023) 107717, https://doi.org/10.1016/j.compositesa.2023.107717.

[22] R.X. Hu, F.H. Zhang, L. Luo, L.L. Wang, Y.J. Liu, J.S. Leng, Chem. Eng. J. 489 (2024) 150956, https://doi.org/10.1016/j.cej.2024.150956.

[23] L.F. Liu, L.J. Li, Y.J. Hu, F.Q. Liu, Y.G. Jiang, J.Z. Feng, J. Feng, Sci. China Mater. 67 (10) (2024) 3347–3357, https://doi.org/10.1007/s40843-024-2987-5.

[24] C. Liu, M.K. Wang, J. Wang, G.Y. Xu, S.Z. Zhang, F. Ding, Small 20 (44) (2024), https://doi.org/10.1002/smll.202404104.

[25] Z. Kantor, T.T. Wu, Z.H. Zeng, S. Gaan, S. Lehner, M. Jovic, A. Bonnin, Z.Y. Pan, Z. Mazrouei-Sebdani, D.M. Opris, M.M. Koebel, W.J. Malfait, S.Y. Zhao, Chem. Eng. J. 443 (2022) 136401, https://doi.org/10.1016/j.cej.2022.136401.

[26] Z.L. Li, L.B. Deng, I.A. Kinloch, R.J. Young, Prog. Mater. Sci. 135 (2023) 101089, https://doi.org/10.1016/j.pmatsci.2023.101089.

[27] S. Rigollet, E. Weiss-Hortala, G. Flamant, A. Nzihou, Chem. Eng. J. 496 (2024), https://doi.org/10.1016/j.cej.2024.153795.

[28] P. Yin, D. Lan, C. Lu, Z. Jia, A. Feng, P. Liu, X. Shi, H. Guo, G. Wu, J. Wang, J. Mater. Sci. Technol. 204 (2025) 204–223, https://doi.org/10.1016/j.jmst.2024.04.007.

[29] B. Jiang, C. Qi, H. Yang, X. Wu, W. Yang, C. Zhang, S. Li, L. Wang, Y. Li, Carbon 208 (2023) 390–409, https://doi.org/10.1016/j.carbon.2023.04.002.

[30] X.J. Zeng, X.Y. Cheng, R.H. Yu, G.D. Stucky, Carbon 168 (2020) 606–623, https://doi.org/10.1016/j.carbon.2020.07.028.

[31] C. Qian, D. Wang, W. Zhao, W. Yang, Z. Qin, Y. Zhu, B. Xu, Mater. Today Nano 23 (2023) 100354, https://doi.org/10.1016/j.mtnano.2023.100354.

[32] X. Xiong, H. Zhang, H. Lv, L. Yang, G. Liang, J. Zhang, Y. Lai, H.-W. Cheng, R. Che, Carbon 219 (2024), https://doi.org/10.1016/j.carbon.2024.118834.

[33] Y.-Y. Wang, F. Zhang, N. Li, J.-F. Shi, L.-C. Jia, D.-X. Yan, Z.-M. Li, Carbon 205 (2023) 10–26, https://doi.org/10.1016/j.carbon.2023.01.007.